


Article

One Bicopper Complex with Good Affinity to Nitrate for Highly Selective Electrocatalytic Nitrate Reduction to Ammonia

Kang-Yu Zeng¹, Jun-Jie Wang^{2,*}, Xiang Fang² and Zuo-Xi Li^{1,*} 

¹ Institute of Materials Science and Devices, School of Material Science and Engineering, Suzhou University of Science and Technology, Suzhou 215009, China

² School of Chemistry and Chemical Engineering and Anyang Key Laboratory of New Functional Complex Materials, Anyang Normal University, Anyang 455000, China

* Correspondence: jjwang@aynu.edu.cn (J.-J.W.); lizx@usts.edu.cn (Z.-X.L.)

Abstract: Ammonia (NH₃) plays an irreplaceable role in human life as a promising energy carrier and indispensable chemical raw material. Nitrate electroreduction to ammonium (NRA) not only removes nitrate pollutants, but also can be used for efficient NH₃ production under ambient conditions. However, achieving high efficiency and selectivity of electrocatalysts is still a great challenge. Herein, a complex Cu₂(NO₃)₄(BMMB)·H₂O with a bicopper core is assembled by Cu(NO₃)₂·3H₂O and 1,4-bis[[2-(2'-pyridyl)benzimidazolyl]methyl]benzene (BMMB) for NRA under alkaline conditions. The optimal sample showed excellent nitrate reduction performance with the NO₃[−] conversion rate of 70%, Faradaic efficiency of up to 90%, and NH₃ selectivity of more than 95%. The high-catalytic activity is mainly due to the ingeniously designed copper cores with strong affinity for NO₃[−], which accelerates the transferring rate of adsorbed nitrate on the Cu surface and increases the efficiency of rate-determining step (NO₃[−] → NO₂[−]) in the whole catalytic process. Therefore, the transformation of surface-exposed nitrate can be rapidly catalyzed by the Cu active sites, facilitating the conversion efficiency of nitrate.

Keywords: electrocatalysts; copper complex; nitrate affinity; nitrate electroreduction; ammonium production



Citation: Zeng, K.-Y.; Wang, J.-J.; Fang, X.; Li, Z.-X. One Bicopper Complex with Good Affinity to Nitrate for Highly Selective Electrocatalytic Nitrate Reduction to Ammonia. *Catalysts* **2022**, *12*, 1561. <https://doi.org/10.3390/catal12121561>

Academic Editor: Jianping Yang

Received: 15 October 2022

Accepted: 25 November 2022

Published: 2 December 2022

Publisher's Note: MDPI stays neutral with regard to jurisdictional claims in published maps and institutional affiliations.



Copyright: © 2022 by the authors. Licensee MDPI, Basel, Switzerland. This article is an open access article distributed under the terms and conditions of the Creative Commons Attribution (CC BY) license (<https://creativecommons.org/licenses/by/4.0/>).

1. Introduction

Currently, water pollution poses a major potential threat to public health and lives. Nitrate (NO₃[−]) plays a non-negligible role among the pollutants [1]. In our daily life, the use of fertilizers, chemical production, and fossil fuels causes massive diffusion of nitrate and nitrogen oxides to surface water and groundwater, which resulted in the water quality not meeting the standard [2,3]. In addition, nitrate can be converted into nitrite (NO₂[−]) in the human body, which causes severe health problems; for instance, gastric cancer and methemoglobin [4–6]. Furthermore, high concentrations of nitrate in the air can lead to acid rain, while in water, high concentrations can contribute to eutrophication [7].

To efficiently denitrify NO₃[−], numerous methods, such as reverse osmosis, adsorption, catalytic reduction, and biological denitrification have been used to treat NO₃[−] [8–11]. However, these techniques have shown some weaknesses. For example, reverse osmosis and adsorption need a post-treatment of highly concentrated NO₃[−], catalytic reduction is costly, biological denitrification is complicated and requires a long time to treat [12]. Electrocatalytic reduction method is more effective to treat nitrate than the above-mentioned methods. In addition, the highly selective reduction product, ammonia (NH₃), can be obtained by an external power supply at room temperature under atmospheric pressure [13–16]. The most desirable product of electrocatalytic nitrate reduction is NH₃, considering that NH₃ is an industrially important raw material and a promising liquefied fuel [17]. Industrial NH₃ is mainly a synthesis using Haber-Bosch process, which operates at high temperature (400~600 °C) and high pressure (>400 atm) [18]. However, NO₃[−] electrocatalytic reduction to valuable NH₃ is an environmentally-friendly, safe, and sustainable

process. According to the reported literatures, the rate-determining step of NRA is the conversion of $\text{NO}_3^- \rightarrow \text{NO}_2^-$; then, the important intermediate NO will be selectively converted into nitrogen or ammonia depending on electrode materials, solution pH, applied voltage, etc. [19–21]. The key point affecting the rate-determining step is the rate of nitrate adsorption on the catalyst surface. Therefore, the suitability of an electrocatalytic material for electrocatalytic nitrate reduction is determined by the ability to effectively adsorb NO_3^- [22]. Among these methods, the NRA technique may be the most suitable for industrial production.

With regard to NRA, electrode materials mainly determine the electrocatalytic performances. At present, noble metal catalysts, such as gold (Au), ruthenium (Ru), and platinum (Pt), have been shown to be excellent electrocatalytic materials [23–28]. Among these materials, although the performance of precious metals is excellent, the cost is expensive and there is no possibility of large-scale use. Transition metals are more suitable materials due to their low price and high electrocatalytic activity and stability. With regard to transition metal catalysts, copper (Cu) is one of the most desirable metals with high Faradaic efficiency (FE) and selectivity toward NH_3 [29,30]. Koper et al. demonstrated that Cu has the highest activity among transition metal catalysts [31]. Wu et al. reported that Cu nanosheets (Cu NSs) have high electric-double-layer-capacitance of 422 mF, indicating a very large electrocatalytic active area. Therefore, Cu NSs exhibit high ammonia selectivity of 99.7% nitrate removal rate [32].

Previous researches declare that some complexes show the ability to produce ammonia by nitrate electrocatalytic reduction. Jakubikowa et al. clarified that $[\text{Co}(\text{DIM})]^{3+}$ (DIM = 2,3-dimethyl-1,4,8,11-tetraazacyclotetradeca-1,3-diene) has an active NO_3^- electrocatalytic reduction to valuable NH_3 , and density functional theory (DFT) was used to study the electronic structure and reaction mechanisms [33]. However, improving the NRA efficiency of complexes is still a challenge. Some efforts have been proposed to improve the catalytic activity. Luo et al. reported that Th-BPYDC (BPYDC = 2,2'-bipyridine-5,5'-dicarboxylic acid) has a low catalytic activity of NRA, but once supported by single-site copper catalyst, it presents $225 \mu\text{mol h}^{-1} \text{cm}^{-2}$ yield and 92.5% Faradaic efficiency for NRA activated at 0.0 V (vs. RHE) [34]. Zhu et al. used an in-situ synthesis method to populate Cu nanoclusters in CuH-HTP (HHTP = 2,3,6,7,10,11-hexahydroxytriphenylene) [35]. In addition, Xu et al. used a similar approach to fill Cu nanoparticles in CeBDC (H_2BDC = 1,4-benzenedicarboxylic acid) [36]. All of these methods are based on the loading of metal particles with a complex carrier, and the active center of catalysis is still the metal particle. Could the initial complexes have good catalytic activity?

With the above assumptions, we proposed a strategy for improving catalytic activity through designing a new complex $\text{Cu}_2(\text{NO}_3)_4(\text{BMMB}) \cdot \text{H}_2\text{O}$ (CuBMMB) with a bicopper core, which exhibits high activity for NRA. Specifically, at -0.53 V vs. reversible hydrogen electrode (RHE), CuBMMB achieves NO_3^- conversion rate and Faradaic efficiency (FE) of up to 70 and 90%, and NH_3 selectivity of more than 95% in 1 M KOH solution with 200 ppm NO_3^- -N. The structure and composition are characterized in detail. To study the selectivity, mass activity, and durability, a combination of characterization tools and electrochemical tests was conducted. Finally, the mechanisms for the significant improvement in electrochemical performance are disclosed.

2. Results and Discussion

2.1. Synthesis of Consideration

First, the semirigid organic 1,4-bis{[2-(2'-pyridyl)benzimidazolyl]methyl}benzene (BMMB) chosen as the desirable ligand is attributed to the fixed bidentate bridging mode, and it makes the coordination with metal ions easier to be regulated (Figure S1). Second, the copper ion possesses good NRA performances. Third, it is important to increase the reaction rate in the rate-determining step ($\text{NO}_3^- \rightarrow \text{NO}_2^-$) of NRA process, and it is a practical strategy to focus on increasing the adsorption efficiency of nitrate on the surface of catalytically active centers. Therefore, we have used copper nitrate as the metal salt,

and successfully achieved good affinity of Cu^{2+} ion with the nitrate ion, which led to the acceleration of the transferring rate of adsorbed nitrate on the Cu surface and improvement of the NRA performances.

2.2. Crystal Structure of CuBMMB

Single-crystal X-ray diffraction analysis reveals that CuBMMB crystallizes in the monoclinic space group $C2/c$ (see Supplementary Material). The asymmetric unit consists of one crystallographically independent Cu^{2+} ion, two nitrate ions, one BMMB ligand, and one free water molecule. As shown in Figure 1, the Cu^{2+} ion is coordinated by two BMMB nitrogen atoms and two nitrate oxygen atoms, which yield a square coordination environment. The Cu–N bond lengths are 1.952(3) and 1.978(3) Å, and the Cu–O bond lengths are 1.968(3) and 1.980(3) Å, which are all comparable to those typically observed values in the related copper complexes. Two terminal groups of BMMB connects one Cu^{2+} ion, and thus each BMMB ligand connects two Cu^{2+} ions. However, the two other coordination sites of Cu^{2+} ion are occupied by the monodentate nitrate ion, which hinders the extension of metal node. Finally, the BMMB ligand connects the Cu^{2+} ion into the complex molecule with a bicopper core.

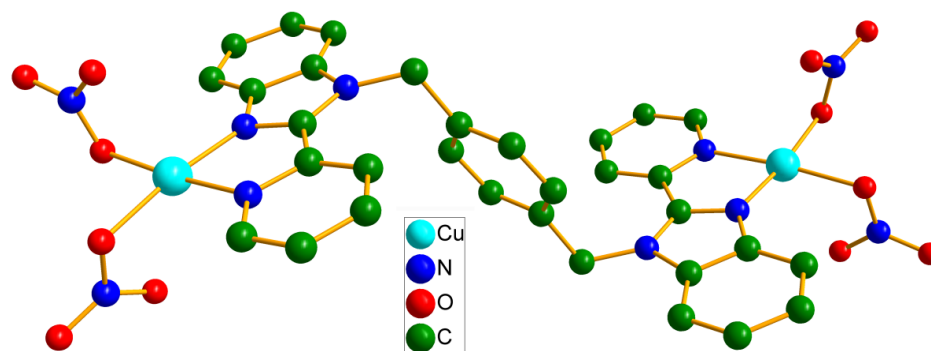


Figure 1. The coordination environment of Cu^{II} ion and bicopper core in CuBMMB.

The X-ray diffraction (XRD) experimental pattern is well-matched with the simulated pattern (Figure 2a), proving the high purity and crystallinity of CuBMMB. With regard to CuBMMB, the distinct peaks at 9.53, 14.57, 18.58, 22.28, and 24.75° can be indexed to the (2 0 2), (4 0 0), (6 0 2), (3 1 2), and (7 1 2) facets. The SEM images (Figures S1 and 2b,c) of CuBMMB present a loose structure with a large number of micron pores on the surface. From the magnified Figure 2b, it can be seen that CuBMMB particles are composed of many small rods with flocculent surfaces interlaced and woven. Not surprisingly, this open porous structure could accelerate the mass transfer of nitrate ions and products. SEM elemental mapping (Figure 2d) of CuBMMB shows that C, N, O, and Cu elements are homogeneously dispersed on the surface of CuBMMB. Energy dispersive X-ray spectroscopy (EDS) (Figure S2) calculates the content of each component and the results are shown in Table S1. The proportions of carbon, nitrogen, oxygen, and copper are 73.25, 4.43, 15.05, and 7.27%, respectively.

There are many identical functional groups in the FT-IR spectrum (Figure 3a) of BMMB and CuBMMB. The peak appearing at 1519 cm^{-1} corresponds to the C=N stretching vibration in the benzimidazole ring, the peaks at 1477 and 3050 cm^{-1} could be identified as the stretching vibration of the benzene ring skeleton [37]. Some peaks correspond to C=C bending modes (1450–1600 cm^{-1}), C–O stretching modes (1200–1250 cm^{-1}), and C–H stretching modes (680–880 cm^{-1}). In particular, the peak at 1350–1400 cm^{-1} corresponds to the –N=C in BMMB. The peak at 1250–1300 cm^{-1} corresponds to the N–O–Cu [38], which matches the results of the O 1s spectrum (Figure S3) of CuBMMB. When the CuBMMB powder was subjected to the TG experiment (Figure 3b), the crystalline water (3.8% observed, 4.0% calculated) was all lost in the region of 81–123 °C. The compounds are stable below 160 °C and decompose rapidly after 160 °C. At 401 °C, a large quantity of carbon

begins to be converted into CO_2 . After almost complete decomposition of carbon at 640°C , the main component of the final product was $\text{Cu}-\text{O}$ with mass of 16.3% (17% calculated). XPS characterization of CuBMMB was carried out to investigate the composition and state of the complex. The XPS pattern for the complex displays the presence of C, N, O, and Cu elements (Figure 3c), which corresponds to the above-mentioned element mapping results. Cu 2p XPS spectra were shown in Figure 3d, and could be divided into three pairs of characteristic peaks of Cu^{2+} , Cu^+/Cu , and satellites [36,39]. A pair of peaks appearing at 934.39 and 954.25 eV accompanied by a pair of satellite peaks at 943 eV ($\text{Cu } 2p_{3/2}$) and 963 eV ($\text{Cu } 2p_{1/2}$) could be attributed to Cu^{2+} [36]. Last pair of peaks at 932.42 eV ($\text{Cu } 2p_{3/2}$) and 952.3 eV ($\text{Cu } 2p_{1/2}$) were assigned to Cu^+/Cu [40,41]. Interestingly, there is a tendency for Cu^{2+} to be reduced to Cu^+/Cu during the synthesis of the complexes, the ratio of Cu^{2+} for CuBMMB (50.22%) is almost the same with Cu^+/Cu ; this phenomenon is consistent with the study by Luo et al. [28]. Furthermore, the high magnification O 1s, C 1s, and N 1s spectra were presented in Figure S3. N 1s spectra are deconvoluted to three peaks of pyridinic-N (398.54 eV), pyrrolic-N (399.86 eV), and Cu-N (405.73 eV) [42], and the contents are 51.9, 30.45, and 17.65%, respectively. The O 1s spectra are fitted to four peaks of H-O (533.3 eV), Cu-O (Cu-O, 532 eV), N-O (532.7 eV), and C-O (531.1 eV) [43,44], and the contents are 11.09, 38.87, 40.98, and 9.06%, respectively; these analyzed bonds correspond to the results of the IR spectra. The relative percentage content regarding each component of multiple nitrogen and oxygen functionalities was listed in Table S1. Complexes containing N- and O- functional groups usually have better wettability and electrical conductivity, which is more conducive to electrocatalytic reactions.

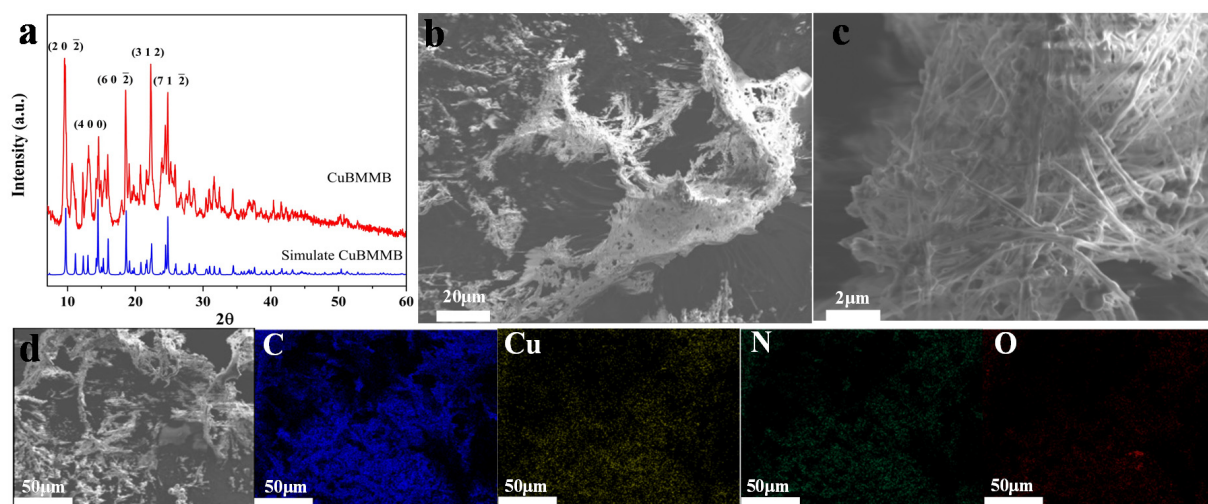


Figure 2. Structure, morphology, and composition analyses: (a) XRD pattern; (b,c) SEM image of CuBMMB; (d) SEM elemental mapping of C, Cu, N, and O in CuBMMB.

A series of electrochemical tests on the NRA properties of CuBMMB were carried out on 660E electrochemical workstation. Cyclic voltammograms (CV), linear sweep voltammetry (LSV), and chronoamperometry (I-t) curves were evaluated via a three-electrode configuration in an H-type electrolytic cell. The CuBMMB, saturated calomel electrode (SCE), and platinum (Pt) foil acted as working electrode, reference electrode, and counter electrode, respectively. The 1 M potassium hydroxide solution (KOH, 40 mL) was respectively added to the anode and cathode chambers, and KNO_3 (200 ppm NO_3^- -N) was added to the cathode chamber. The transformation of NO_3^- to NH_3 was investigated over a reaction time of 5 h via the potentiostatic method with different potentials. The reductive products (NO_3^- -N, NO_2^- -N, NH_4^+ -N) were determined by colorimetric methods, and the calibration curves were depicted in Figure S4. As shown in the Cu coordination environment (Figure 1), the coordinated NO_3^- and the NO_3^- on the surface of the electrode material could be converted to NO_2^- with the electrochemical reaction. The

total nitrogen content in the solution could gradually increase with time, and reach 208.7 ppm after 5 h (Table S2). In view of this situation, we use the changed NO_3^- concentration when calculating the NO_3^- removal efficiency, Faradaic efficiency, and selectivity toward NH_3 . As shown in Figure 4a, the LSV curves of CuBMMB showed a rapid increase in current density with the presence of NO_3^- , indicating that CuBMMB has the activity to catalyze the NO_3^- reduction. Moreover, NRA performance of carbon cloth was investigated (Figures S5 and S6), and showed that carbon cloth exhibited significant lower efficiency in catalyzing the NO_3^- reduction than CuBMMB in the potential window. Furthermore, the NO_3^- conversion rate and FE were significantly lower than CuBMMB. Therefore, it can be concluded that the carbon cloth has little effect on the NRA performance of CuBMMB. The NRA performance of CuBMMB at different potentials (-0.63 , -0.53 , -0.43 , and -0.33 V vs. RHE) was investigated. As displayed in Figure 4b, the nitrate removal efficiency gradually increased with the improvement in potential and achieved the maximum value of 89% at -0.63 V. However, Faradaic efficiency toward NH_3 production is lowest at 61.4%, which was mainly due to the competing HER, as it played a dominant role at high potential. At -0.53 V, Faradaic efficiency was around 90%, NO_3^- removal efficiency was 73.4%, NH_4^+ selectivity and ammonia yield rate were 96.5% and $77 \mu\text{mol h}^{-1} \text{cm}^{-2}$, with almost no NO_2^- in the products (Figure 4c). In addition to the colorimetric methods, the concentration of products was verified using ion chromatography (Figures S7–S9). The calculated concentrations from ion chromatography were almost the same as the colorimetric method (Table S3). As the reaction proceeds, the concentration of NH_4^+ gradually increased, while the concentration of NO_3^- decreased, suggesting the reaction of $\text{NO}_3^- \rightarrow \text{NH}_4^+$ (Figure S10). After 5 h of reaction, the conversion rate of NO_3^- became flat, and the growth rate of NH_4^+ also decreased, implying that the reaction on the surface of CuBMMB reached equilibrium. The results of time-dependent product contents showed that more than 70% of NO_3^- had converted to NH_4^+ and NO_2^- , where the NH_3 selectivity was 96.5%. The catalytic performance of CuBMMB at different concentrations (50, 100, 200, and 400 ppm) was also investigated, and the LSV curves for each condition were shown in Figure 4d. There is no doubt that the current density increased faster as the nitrate concentration increased. As shown in Figure 4e, the FE of NH_4^+ production reached a maximum value (97%) at 100 ppm NO_3^- -N, and the 400 ppm NO_3^- -N reached the minimum value (71.7%). Moreover, the impact on selectivity of NH_3 production was studied with all NO_3^- -N concentrations, and the values reached the maximum value (96.5%) at 200 ppm NO_3^- -N. Stability is a crucial factor for electrocatalysts in practical applications. As presented in Figure 4f, FE and NO_3^- conversion rate showed a significant decrease after three consecutive cycles (each cycle lasts 5 h). Due to the coordination of Cu with nitrate, which leads to an unstable material surface during the electrochemical process, the material surface inevitably reconfigures as the reaction time increases, which leads to the exposure of more active sites and acceleration of the hydrogen evolution reaction; therefore, further destroying the crystal structure of the complex. The number of active sites has an important influence on the activity of electrocatalyst. As a result, electrochemical active surface areas (ECSA) were derived from double-layer capacitances (C_{dl}), which was determined by the functional relationship between capacitive currents and scan rates (Figure S11). The results of linear fitting indicated that the specific capacitance of CuBMMB was 0.28 mF cm^{-2} . Tafel plot obtained from the LSV curves in 1 M KOH electrolyte with 200 ppm NO_3^- -N was shown in Figure S12, with CuBMMB exhibiting a modest Tafel slope of $228.9 \text{ mV dec}^{-1}$.

Characterization of the composition and structure of the CuBMMB after the NRA were conducted by SEM, XRD, and XPS in Figure 5. According to the SEM image (Figure 5a) of the CuBMMB after the reaction, the surface of the material was clearly reconstructed. The small, clear holes on the surface before the reaction have turned into craters, and the spread-out layers have gathered into blocks. Moreover, the XRD image (Figure 5b) proved that the crystal structure of CuBMMB was destroyed. The FE and NO_3^- conversion rate dropped significantly after three cycles, which was mainly due to the competing HER. By comparing Figure 2c with Figure 5a, we can infer that the disruption of the

CuBMMB structure exposes a large number of active sites and breaks the equilibrium between the HER and NRA reactions, which significantly facilitates the HER reaction. Therefore, an increasing number of bubbles exist on the material surface with the reaction. With regard to the high-resolution XPS spectra of Cu 2p (Figure 5c), compared to the initial complex, the Cu 2p_{1/2} spectra exhibit a slight negative shift, demonstrating that the copper ions in the complex become more stable after NRA, with an increase in the content of Cu²⁺ (50.22 → 55.48%) [45]. However, two peaks (292.5 and 295.5 eV) at high binding energies in the spectra of C 1s after NRA (Figure S13) indicate a disruption in the material structure, which is consistent with the XRD and SEM characterization findings. The rate-determining step reaction ($\text{NO}_3^-_{(\text{ad})} \rightarrow \text{NO}_2^-_{(\text{ad})}$) first adsorbs $\text{NO}_3^-_{(\text{aq})}$ on the surface of the electrocatalytic material to form $\text{NO}_3^-_{(\text{ad})}$, and then obtains electrons to generate $\text{NO}_2^-_{(\text{ad})}$ [18]. The electron transfer step is very fast, and the key point is the adsorption of NO_3^- . Notably, benefiting from the straightforward and efficient design approach, the adsorption capacity of Cu ions for NO_3^- is greatly increased, thus accelerating the rate-determining step $\text{NO}_3^- + \text{H}_2\text{O} + 2\text{e}^- \rightarrow \text{NO}_2^- + 2\text{OH}^-$ and converting almost all of the NO_2^- adsorbed to NH_4^+ ($\text{NO}_2^- + 8\text{H}^+ + 6\text{e}^- \rightarrow \text{NH}_4^+ + 2\text{H}_2\text{O}$) (Figure 5d). The electrocatalytic activity of CuBMMB (initial coordination polymer) is comparable to the MOF-loaded metal particle catalysts (Table S4).

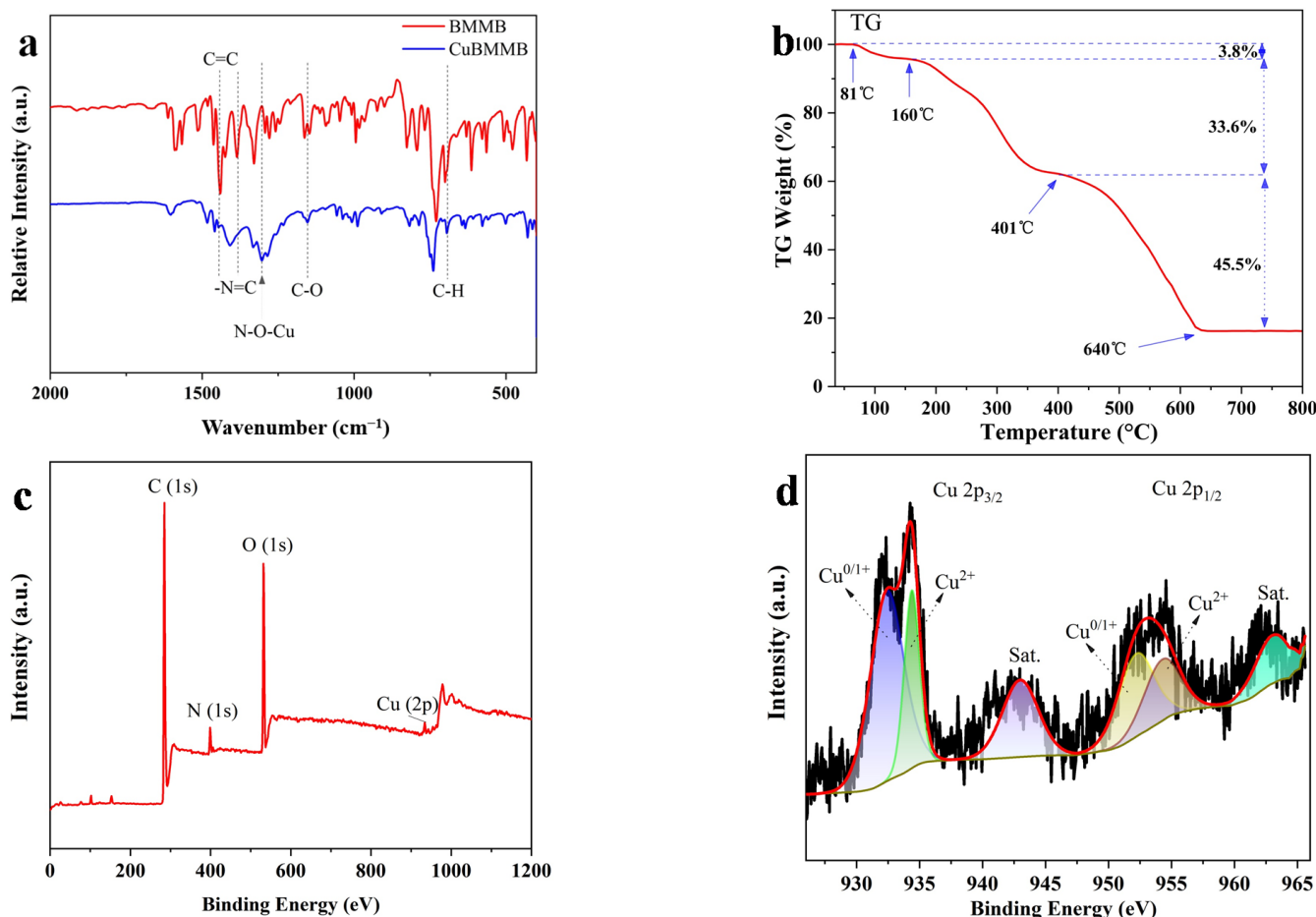


Figure 3. (a) FT-IR; (b) TG spectra of CuBMMB; and XPS survey of (c) CuBMMB and (d) Cu 2p.

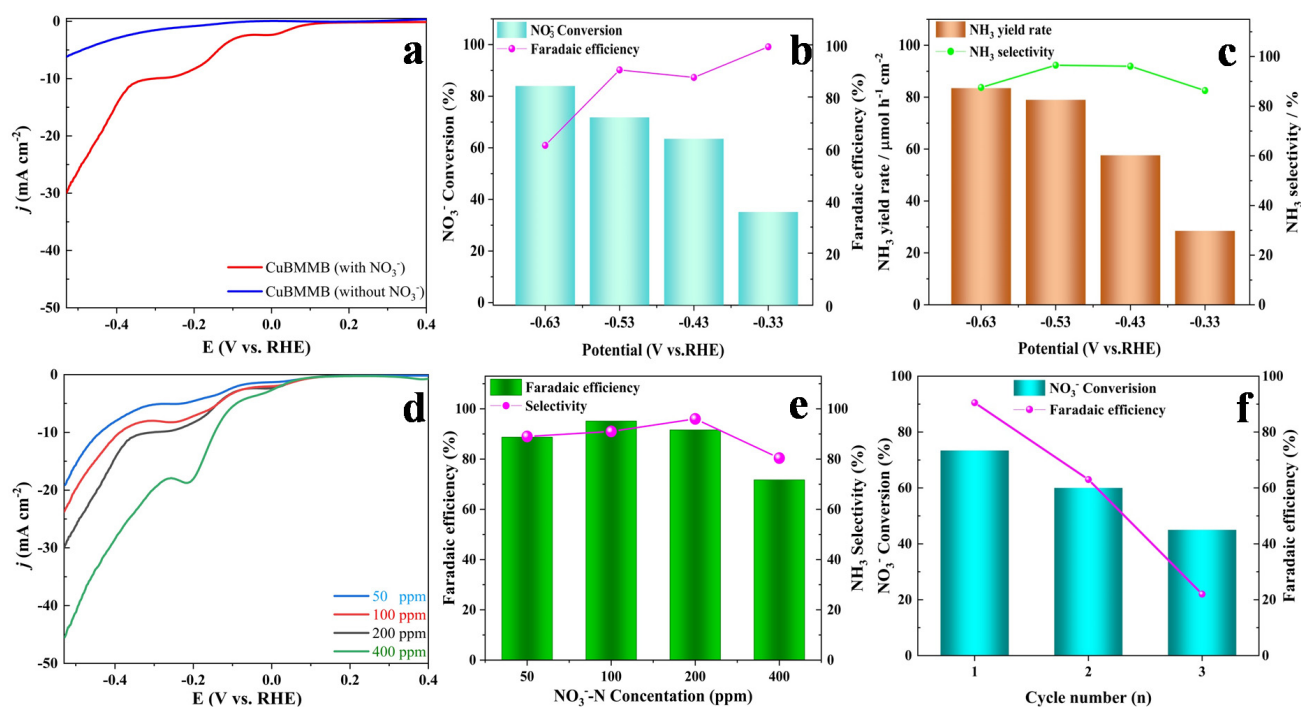


Figure 4. NRA electrocatalytic performance. (a) LSV curves of CuBMMB in 1 M KOH electrolyte with and without NO_3^- , respectively; (b) potential–dependent FE and selectivity of NH_3 over CuBMMB in 1 M KOH electrolyte with 200 ppm NO_3^- ; (c) NH_3 yield rate and NH_3 selectivity of CuBMMB electrodes under different potentials; (d) LSV curves of CuBMMB tested with different NO_3^- -N concentrations; (e) FE and selectivity of NH_3 tested at -0.53 V vs. RHE over CuBMMB in 1 M KOH electrolyte with 50, 100, 200, and 400 ppm NO_3^- -N concentrations; (f) the consecutive recycling test of CuBMMB at -0.53 V vs. RHE 1 M KOH electrolyte with 200 ppm NO_3^- .

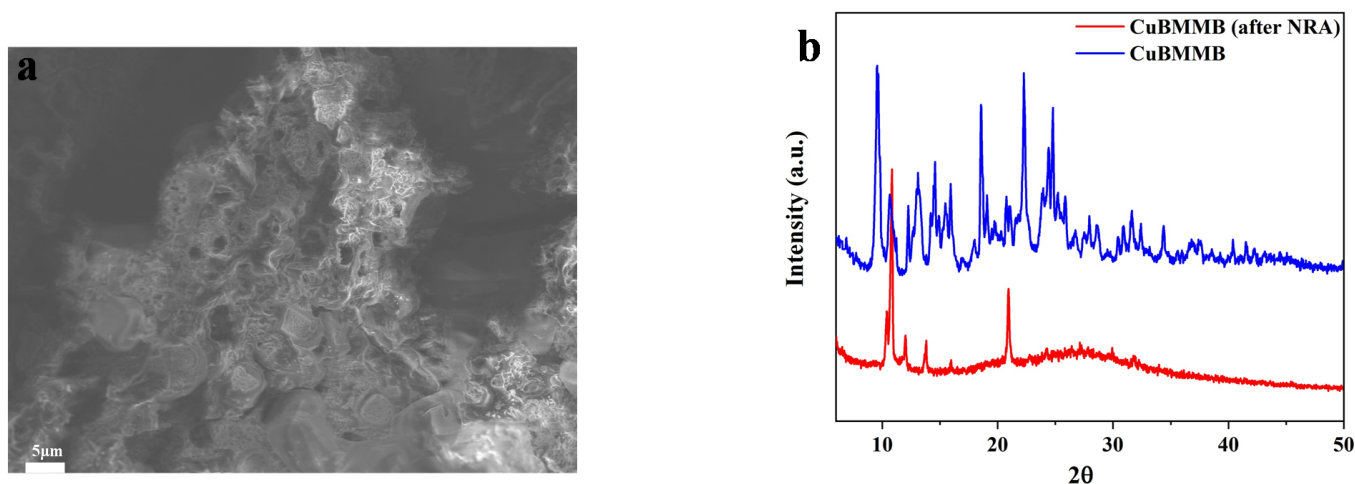


Figure 5. Cont.

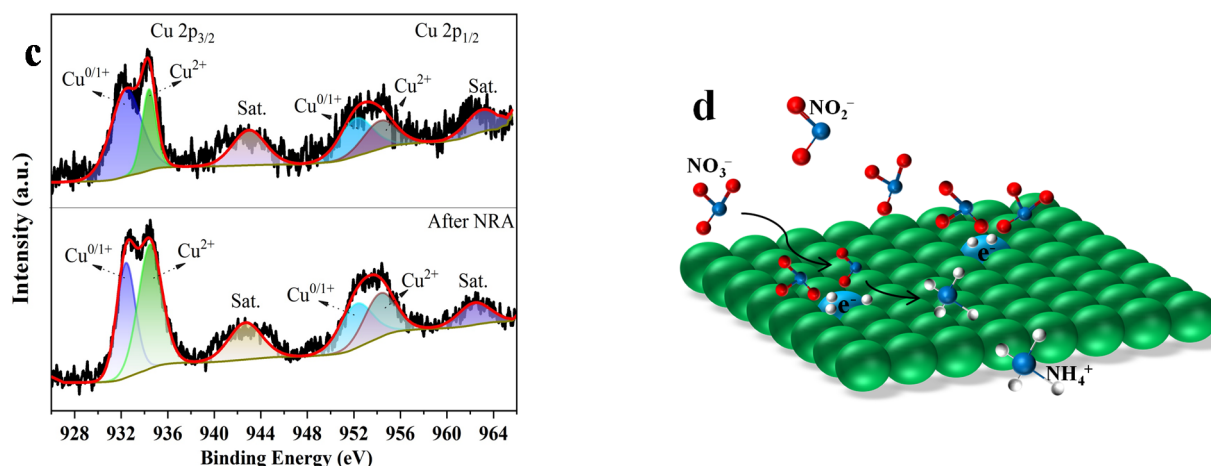


Figure 5. Structure, morphology, and composition analysis after NRA; (a) SEM; (b) XRD; (c) and XPS spectra of CuBMMB; (d) proposed electrochemical process involved in the nitrate reduction in CuBMMB.

3. Materials and Methods

3.1. Synthesis of CuBMMB Crystals and Powder

All solvents and reagents for the synthesis were commercially available and used as received. The CuBMMB crystals were synthesized by the solvent-diffusing method. First, 6 mL methanol (CH_3OH) solution of $\text{Cu}(\text{NO}_3)_2 \cdot x\text{H}_2\text{O}$ (0.1 mmol) was added dropwise at the bottom of a test tube. Then, the solution of CH_3OH and CHCl_3 (1:1.8 mL) was carefully added as a buffer layer. Finally, a solution of 1,4-bis{[2-(2'-pyridyl)benzimidazolyl]methyl}benzene (BMMB) in CHCl_3 (6 mL) was layered onto the buffer layer, and the test tube was then arranged at an undisturbed place. After ~3 weeks, green single crystals appeared on the wall of the test tube.

The Cu-MOF powder was synthesized as follows. The ligand BMMB and $\text{Cu}(\text{NO}_3)_2 \cdot x\text{H}_2\text{O}$ were dissolved in CHCl_3 and CH_3OH to obtain a clear solution, respectively. Subsequently, the two clear liquids were mixed and stirred at room temperature for 12 h. Then, the green powder precipitated and thereafter was centrifuged and rinsed with deionized water and ethanol several times. Finally, the powder was evacuated at 60°C under vacuum for 6 h.

3.2. Characterization

X-ray diffraction (XRD) was recorded with Bruker D8 Advance powder XRD system (Billerica, MA, USA) using $\text{Cu K}\alpha$ radiation ($\lambda = 1.54 \text{ \AA}$). IR spectra were recorded on Thermo-Nicolet 6700 (Thermo Fischer Scientific, Kandel, Germany) with air as a reference. Field emission scanning electron microscopy (FE-SEM, Hitachi SU8010, Tokyo, Japan) has been utilized to obtain morphology information on the samples. X-ray photoelectron spectroscopy (XPS) survey was performed on Thermo Fisher ESCALAB Xi+ instrument and the non-monochromatized Al-Ka X-ray was used. Thermogravimetry analysis was conducted on METTERLER under air atmosphere with the heating rate of 5°C min^{-1} in the range of $35\text{--}800^\circ\text{C}$.

3.3. Electrochemical Measurements

Electrochemical measurements were conducted on a CHI 660E electrochemical workstation (Chinstruments, Shanghai, China) using an H-type electrolytic cell separated by a membrane (Nafion-117). Saturated calomel electrode (SCE), Pt foil electrode, and as-prepared electrode were used as reference electrode, counter electrode, and working electrode, respectively. The 1 M KOH solution (40 mL) with different concentrations of KNO_3 was used in the cathode (containing 200 ppm nitrate-N) and anode (containing 0 ppm nitrate-N) compartments. Linear sweep voltammetry (LSV) was performed at a scan rate of

10 mV s^{−1} to obtain polarization curves from 0.40 to −0.53 V (vs. RHE). The potentiostatic curve tests were performed at different potentials (−0.33, −0.43, −0.53, and −0.63 V vs. RHE) for 5 h with a stirring rate of 300 rpm. The electrochemical double-layer capacitance (C_{dl}) using the cyclic voltammetry (CV) method was nearly a non-Faradaic potential window (from 0.97 to 1.07 V) at different scan rates of 10, 20, 40, 60, 80, 100 mV s^{−1}. The concentrations of nitrate-N, nitrite-N, and ammonia-N were detected by UV–Vis spectrophotometry (Shimadzu UV-2600i) according to the standard method. Meanwhile, the concentrations of ammonia-N were also confirmed by ion chromatography (Shine CIC-D100). The detailed determination methods are provided in the Supporting Information (SI).

4. Conclusions

In summary, the coordination polymer CuBMMB proved to be a novel NRA electrocatalyst with outstanding activity, good nitrate conversion rate, high NH₃ selectivity, and FE of NH₃. Under the desirable potential of −0.53 V vs. RHE, CuBMMB in alkaline conditions showed excellent nitrate reduction performance with the NO₃[−] conversion rate of 70%, Faradaic efficiency of up to 90%, and NH₃ selectivity of more than 95%. This high-catalytic activity is mainly due to the ingeniously designed copper cores with strong affinity for NO₃[−], which accelerates the transferring rate of adsorbed nitrate on the Cu surface and increases the efficiency of rate-determining step (NO₃[−] → NO₂[−]) for the whole catalytic process. Therefore, the transformation of surface-exposed nitrate can be rapidly catalyzed by the Cu active sites, and the high affinity of Cu ion for nitrate greatly promotes the efficiency of nitrate conversion.

Supplementary Materials: The following supporting information can be downloaded at: <https://www.mdpi.com/article/10.3390/catal12121561/s1>; Figure S1: SEM image of the CuBMMB; Figure S2: The EDS images of the CuBMMB; Figure S3: The XPS survey of C 1s, N 1s, and O 1s; Figure S4: Concentration-absorbance calibration curves of (a) ammonia-N, (b) nitrate-N, and (c) nitrite-N; Figure S5: LSV curves in 1 M KOH electrolyte with 200 ppm NO₃[−]-N; Figure S6: Faradaic efficiency and nitrate conversion of the CuBMMB and carbon cloth in 1 M KOH electrolyte with 200 ppm NO₃[−]-N at −0.53 V (vs. RHE); Figure S7: Ion chromatogram (IC) curves of the time-dependent ammonium production for a series of standard ammonium solutions and CuBMMB at −0.53 V; (b) calibration curve of IC for ammonium concentration; Figure S8: IC curves of the time-dependent nitrate residue for a series of standard nitrate solutions and CuBMMB at −0.53 V; (b) calibration curve of IC for nitrate concentration; Figure S9: IC curves of the time-dependent nitrite production for a series of standard nitrite solutions and CuBMMB at −0.53 V; (b) calibration curve of IC for nitrite concentration; Figure S10: Time-dependent concentration of NO₃[−], NO₂[−], and NH₄⁺ over CuBMMB at −0.53 V vs. RHE; Figure S11: (a) CV curves of the CuBMMB at different scanning rates (10–100 mV s^{−1}); (b) relationship between the scanning rate and the current density of Cu-MOF; Figure S12: Tafel plot of CuBMMB in 1 M KOH electrolyte with 200 ppm NO₃[−]-N; Figure S13: The XPS survey of C 1s, N 1s, and O 1s after NRA; Table S1: The element distribution of CuBMMB; Table S2: The value of total nitrogen element at different times; Table S3: The value of ion chromatography and colorimetric methods for the concentration of produced nitrite and ammonium as well as residual nitrate; Table S4: Performance comparison; References [3,5,24,25,29,30,34–36] are cited in Supplementary Materials.

Author Contributions: Z.-X.L. conceived the idea, discussed results and revised the manuscript. J.-J.W. analysed crystal data and revised the manuscript. K.-Y.Z. tested electrochemical data, discussed results and prepared the manuscript. X.F. performed syntheses. All authors have read and agreed to the published version of the manuscript.

Funding: This work was supported by the National Natural Science Foundation of China (21673177, 22171205).

Data Availability Statement: Data openly available in a public repository, which can be free downloaded in the website of mdpi system.

Acknowledgments: K.Y.Z. thanks Feng Du for his assistance in the measurements and discussion of NRA.

Conflicts of Interest: The authors declare no conflict of interest.

References

- Chen, T.; Li, Y.; Li, L.; Zhao, Y.; Shi, S.; Jiang, R.; Ma, H. Cu Modified Pt Nanoflowers with Preferential (100) Surfaces for Selective Electroreduction of Nitrate. *Catalysts* **2019**, *9*, 536. [\[CrossRef\]](#)
- Shi, Z.; Wang, F.; Xiao, Q.; Yu, S.; Ji, X. Selective and Efficient Reduction of Nitrate to Gaseous Nitrogen from Drinking Water Source by UV/Oxalic Acid/Ferric Iron Systems: Effectiveness and Mechanisms. *Catalysts* **2022**, *12*, 348. [\[CrossRef\]](#)
- Eaton, A.D.; Clesceri, L.S.; Greenberg, A.E.; Franson, M.A.H. Standard methods for the examination of water and wastewater. *Am. J. Public Health Nations Health* **1966**, *56*, 387–388.
- Sanchis, I.; Rodriguez, J.J.; Mohedano, A.F.; Diaz, E. Activity and Stability of Pd Bimetallic Catalysts for Catalytic Nitrate Reduction. *Catalysts* **2022**, *12*, 729. [\[CrossRef\]](#)
- Wang, Y.; Yu, Y.; Jia, R.; Zhang, C.; Zhang, B. Electrochemical Synthesis of Nitric Acid from Air and Ammonia through Waste Utilization. *Natl. Sci. Rev.* **2019**, *6*, 730. [\[CrossRef\]](#) [\[PubMed\]](#)
- Zhang, R.; Liu, H.; Jiang, W.; Liu, W. Ordered Mesoporous nZVI/Zr-Ce-SBA-15 Catalysts Used for Nitrate Reduction: Synthesis, Optimization and Mechanism. *Catalysts* **2022**, *12*, 797. [\[CrossRef\]](#)
- Zou, X.; Chen, C.; Wang, C.; Zhang, Q.; Yu, Z.; Wu, H.; Zhuo, C.; Zhang, T.C. Combining electrochemical nitrate reduction and anammox for treatment of nitrate-rich wastewater: A short review. *Sci. Total Environ.* **2021**, *800*, 149645. [\[CrossRef\]](#)
- Kim, D.G.; Hwang, Y.H.; Shin, H.S.; Ko, S.O. Kinetics of nitrate adsorption and reduction by nano-scale zero valent iron (NZVI): Effect of ionic strength and initial pH. *KSCE J. Civ. Eng.* **2015**, *20*, 175–187. [\[CrossRef\]](#)
- Labarca, F.; Bórquez, R. Comparative study of nanofiltration and ion exchange for nitrate reduction in the presence of chloride and iron in groundwater. *Sci. Total Environ.* **2020**, *723*, 137809. [\[CrossRef\]](#)
- Sheydaei, M.; Ayoubi-Feiz, B. Nitrate reduction through the visible-light photoelectrocatalysis and photoelectrocatalysis/reverse osmosis processes: Assessment of graphene/Ag/N-TiO₂ nanocomposite. *J. Water Process Eng.* **2021**, *39*, 101856. [\[CrossRef\]](#)
- Zhang, W.; Bai, Y.; Ruan, X.; Yin, L. The biological denitrification coupled with chemical reduction for groundwater nitrate remediation via using SCCMs as carbon source. *Chemosphere* **2019**, *234*, 89–97. [\[CrossRef\]](#) [\[PubMed\]](#)
- Tokazhanov, G.; Ramazanov, E.; Hamid, S.; Bae, S.; Lee, W. Advances in the catalytic reduction of nitrate by metallic catalysts for high efficiency and N₂ selectivity: A review. *Chem. Eng. J.* **2020**, *384*, 123252. [\[CrossRef\]](#)
- Shi, M.M.; Bao, D.; Wulan, B.R.; Li, Y.H.; Zhang, Y.F.; Yan, J.M.; Jiang, Q. Au Sub-Nanoclusters on TiO₂ toward Highly Efficient and Selective Electrocatalyst for N₂ Conversion to NH₃ at Ambient Conditions. *Adv. Mater.* **2017**, *29*, 1606550. [\[CrossRef\]](#) [\[PubMed\]](#)
- Luo, Y.; Chen, G.F.; Ding, L.; Chen, X.; Ding, L.X.; Wang, H. Efficient Electrocatalytic N₂ Fixation with MXene under Ambient Conditions. *Joule* **2019**, *3*, 279–289. [\[CrossRef\]](#)
- Yu, X.; Han, P.; Wei, Z.; Huang, L.; Gu, Z.; Peng, S.; Ma, J.; Zheng, G. Boron-Doped Graphene for Electrocatalytic N₂ Reduction. *Joule* **2018**, *2*, 1610–1622. [\[CrossRef\]](#)
- Lv, C.; Yan, C.; Chen, G.; Ding, Y.; Sun, J.; Zhou, Y.; Yu, G. An Amorphous Noble-Metal-Free Electrocatalyst that Enables Nitrogen Fixation under Ambient Conditions. *Angew. Chem. Int. Ed.* **2018**, *130*, 6181–6184. [\[CrossRef\]](#)
- Jung, W.; Hwang, Y.J. Material strategies in the electrochemical nitrate reduction reaction to ammonia production. *Mater. Chem. Front.* **2021**, *5*, 6803–6823. [\[CrossRef\]](#)
- Wang, J.; Feng, T.; Chen, J.; Ramalingam, V.; Li, Z.; Kabtamu, D.M.; He, J.-H.; Fang, X. Electrocatalytic nitrate/nitrite reduction to ammonia synthesis using metal nanocatalysts and bio-inspired metalloenzymes. *Nano Energy* **2021**, *86*, 106088. [\[CrossRef\]](#)
- Garcia-Segura, S.; Lanzarini-Lopes, M.; Hristovski, K.; Westerhoff, P. Electrocatalytic reduction of nitrate: Fundamentals to full-scale water treatment applications. *Appl. Catal. B Environ.* **2018**, *236*, 546–568. [\[CrossRef\]](#)
- Su, J.F.; Ruzybayev, I.; Shah, I.; Huang, C.P. The electrochemical reduction of nitrate over micro-architected metal electrodes with stainless steel scaffold. *Appl. Catal. B Environ.* **2016**, *180*, 199–209. [\[CrossRef\]](#)
- Huang, J.; Zhang, Q.; Ding, J.; Zhai, Y. Fe–N–C single atom catalysts for the electrochemical conversion of carbon, nitrogen and oxygen elements. *Mater. Rep. Energy* **2022**, *2*, 100141. [\[CrossRef\]](#)
- Katsounaros, I.; Kyriacou, G. Influence of nitrate concentration on its electrochemical reduction on tin cathode: Identification of reaction intermediates. *Electrochim. Acta* **2008**, *53*, 5477–5484. [\[CrossRef\]](#)
- Polatides, C.; Kyriacou, G. Electrochemical reduction of nitrate ion on various cathodes-reaction kinetics on bronze cathode. *J. Appl. Electrochem.* **2005**, *35*, 421–427. [\[CrossRef\]](#)
- Jiang, M.; Su, J.; Song, X.; Zhang, P.; Zhu, M.; Qin, L.; Jin, Z. Interfacial Reduction Nucleation of Noble Metal Nanodots on Redox-Active Metal–Organic Frameworks for High-Efficiency Electrocatalytic Conversion of Nitrate to Ammonia. *Nano Lett.* **2022**, *22*, 2529–2537. [\[CrossRef\]](#) [\[PubMed\]](#)
- Qin, J.; Wu, K.; Chen, L.; Wang, X.; Zhao, Q.; Liu, B.; Ye, Z. Achieving high selectivity for nitrate electrochemical reduction to ammonia over MOF-supported Ru_xO_y clusters. *J. Mater. Chem. A* **2022**, *10*, 3963–3969. [\[CrossRef\]](#)
- Li, J.; Zhan, G.; Yang, J.; Quan, F.; Mao, C.; Liu, Y.; Wang, B.; Lei, F.; Li, L.; Chan, A.W.M.; et al. Efficient Ammonia Electrosynthesis from Nitrate on Strained Ruthenium Nanoclusters. *J. Am. Chem. Soc.* **2020**, *142*, 7036–7046. [\[CrossRef\]](#)
- Chen, T.; Li, H.; Ma, H.; Koper, M.T. Surface Modification of Pt(100) for Electrocatalytic Nitrate Reduction to Dinitrogen in Alkaline Solution. *Langmuir* **2015**, *31*, 3277–3281. [\[CrossRef\]](#)
- Hasnat, M.A.; Ahamad, N.; Uddin, S.N.; Mohamed, N. Silver modified platinum surface/H⁺ conducting Nafion membrane for cathodic reduction of nitrate ions. *Appl. Surf. Sci.* **2012**, *258*, 3309–3314. [\[CrossRef\]](#)

29. Wang, Y.; Xu, A.; Wang, Z.; Huang, L.; Li, J.; Li, F.; Wicks, J.; Luo, M.; Nam, D.-H.; Tan, C.-S. Enhanced Nitrate-to-Ammonia Activity on Copper–Nickel Alloys via Tuning of Intermediate Adsorption. *J. Am. Chem. Soc.* **2020**, *142*, 5702–5708. [[CrossRef](#)]
30. Li, J.; Gao, J.; Feng, T.; Zhang, H.; Liu, D.; Zhang, C.; Guo, C. Effect of supporting matrixes on performance of copper catalysts in electrochemical nitrate reduction to ammonia. *J. Power Sources* **2021**, *511*, 230463. [[CrossRef](#)]
31. Dima, G.E.; De Vooys, A.C.A.; Koper, M.T.M. Electrocatalytic reduction of nitrate at low concentration on coinage and transition-metal electrodes in acid solutions. *J. Electroanal. Chem.* **2003**, *554–555*, 15–23. [[CrossRef](#)]
32. Wu, T.; Kong, X.; Tong, S.; Chen, Y.; Liu, J.; Tang, Y.; Yang, X.; Chen, Y.; Wan, P. Self-supported Cu nanosheets derived from CuCl–CuO for highly efficient electrochemical degradation of NO_3^- . *Appl. Surf. Sci.* **2019**, *489*, 321–329. [[CrossRef](#)]
33. Kwon, H.Y.; Braley, S.E.; Madriaga, J.P.; Smith, J.M.; Jakubikova, E. Electrocatalytic nitrate reduction with Co-based catalysts: Comparison of DIM, TIM and cyclam ligands. *Dalton Trans.* **2021**, *50*, 12324–12331. [[CrossRef](#)]
34. Gao, Z.; Lai, Y.; Tao, Y.; Xiao, L.; Zhang, L.; Luo, F. Constructing Well-Defined and Robust Th-MOF-Supported Single-Site Copper for Production and Storage of Ammonia from Electroreduction of Nitrate. *ACS Cent. Sci.* **2021**, *7*, 1066–1072. [[CrossRef](#)]
35. Zhu, X.; Huang, H.; Zhang, H.; Zhang, Y.; Shi, P.; Qu, K.; Cheng, S.-B.; Wang, A.-L.; Lu, Q. Filling Mesopores of Conductive Metal–Organic Frameworks with Cu Clusters for Selective Nitrate Reduction to Ammonia. *ACS Appl. Mater. Interfaces* **2022**, *14*, 32176–32182. [[CrossRef](#)] [[PubMed](#)]
36. Xu, Y.T.; Xie, M.Y.; Zhong, H.; Cao, Y. In Situ Clustering of Single-Atom Copper Precatalysts in a Metal–Organic Framework for Efficient Electrocatalytic Nitrate-to-Ammonia Reduction. *ACS Catal.* **2022**, *12*, 8698–8706. [[CrossRef](#)]
37. Lee, S.Y.; Jung, H.; Kim, N.K.; Oh, H.S.; Min, B.K.; Hwang, Y.J. Mixed Copper States in Anodized Cu Electrocatalyst for Stable and Selective Ethylene Production from CO_2 Reduction. *J. Am. Chem. Soc.* **2018**, *140*, 8681–8689. [[CrossRef](#)] [[PubMed](#)]
38. Mao, H.; Xu, J.; Hu, Y.; Huang, Y.; Song, Y. The effect of high external pressure on the structure and stability of MOF $\alpha\text{-Mg}_3(\text{HCOO})_6$ probed by in situ Raman and FT-IR spectroscopy. *J. Mater. Chem. A* **2015**, *3*, 11976–11984. [[CrossRef](#)]
39. Zhang, D.F.; Zhang, H.; Guo, L.; Zheng, K.; Han, X.D.; Zhang, Z. Delicate control of crystallographic facet-oriented Cu_2O nanocrystals and the correlated adsorption ability. *J. Mater. Chem.* **2009**, *19*, 5220–5225. [[CrossRef](#)]
40. Yang, L.; Li, J.; Du, F.; Gao, J.; Liu, H.; Huang, S.; Zhang, H.; Li, C.; Guo, C. Interface engineering cerium-doped copper nanocrystal for efficient electrochemical nitrate-to-ammonia production. *Electrochim. Acta* **2022**, *411*, 140095. [[CrossRef](#)]
41. Xu, H.; Wu, J.; Luo, W.; Li, Q.; Zhang, W.; Yang, J. Dendritic Cell-Inspired Designed Architectures toward Highly Efficient Electrocatalysts for Nitrate Reduction Reaction. *Small* **2020**, *16*, 2001775. [[CrossRef](#)] [[PubMed](#)]
42. Tolman, C.A.; Riggs, W.M.; Linn, W.J.; King, C.M.; Wendt, R.C. Electron spectroscopy for chemical analysis of nickel compounds. *Inorg. Chem.* **1973**, *12*, 2770–2778. [[CrossRef](#)]
43. Nangan, S.; Ding, Y.; Alhakemy, A.Z.; Liu, Y.; Wen, Z. Hybrid alkali-acid urea-nitrate fuel cell for degrading nitrogen-rich wastewater. *Appl. Catal. B: Environ.* **2021**, *286*, 119892. [[CrossRef](#)]
44. Nefedov, V.I.; Salyn, Y.V.; Leonhardt, G.; Scheibe, R. A comparison of different spectrometers and charge corrections used in X-ray photoelectron spectroscopy. *J. Electron Spectrosc. Relat. Phenom.* **1977**, *10*, 121–124. [[CrossRef](#)]
45. Du, F.; Li, J.; Wang, C.; Yao, J.; Tan, Z.; Yao, Z.; Li, C.; Guo, C. Active sites-rich layered double hydroxide for nitrate-to-ammonia production with high selectivity and stability. *Chem. Eng. J.* **2022**, *434*, 14641. [[CrossRef](#)]